Internal Losses and Flow Behavior of a Turbofan Stage at Windmill

Dilip Prasad

Wesley K. Lord

Aerodynamics Division,
Pratt and Whitney Aircraft Engines,
East Hartford, CT 06108

The flow through a high-bypass ratio fan stage during engine-out conditions is investigated, with the objective of quantifying the internal losses when the rotor is at "windmill." An analysis of altitude test data at various simulated flight Mach numbers shows that the fan rotational speed scales with the engine mass flow rate. Making use of the known values of the nozzle coefficients, we deduce the stagnation pressure loss of the fan stage, which rises significantly as the mass flow rate increases. In order to better understand this behavior, numerical simulations of the fan stage were carried out. The calculated losses agree well with the test data, and it is found that the bulk of the stagnation pressure loss occurs in the stator. A detailed examination of the flow field reveals that the relative flow leaves the rotor at very nearly the metal angle. Moreover, the rotational speed of the fan is such that the inboard sections of the fan blade add work to the flow, while the outboard sections extract work from it. The overall work is essentially zero so that the absolute swirl angle at the rotor exit is small, causing the stator to operate at a severely negative incidence. A gross separation ensues, and the resulting blockage of the stator passage accelerates the flow to high Mach numbers. The highly separated flow in the vane, together with the mixing of the large wakes behind it are responsible for the high losses in the vane. Based on the simulation results for the flow behavior, a simple physical model to estimate the windmill speed of the rotor is developed and is found to be in good agreement with the test data. The utility of this model is that it enables the development of a procedure to predict the internal drag at engine-out conditions, which is discussed.

[DOI: 10.1115/1.3147106]

1 Introduction

[1]An important consideration in the design of nacelles for commercial aircraft engines is the propulsion system drag at engine-out "windmill" conditions, where the fan rotor is in a freewheeling mode. Under these conditions, the mass flow ratio is considerably lower than when the engine is operational, causing significant flow spillage over the nacelle leading edge. If the nacelle were designed purely for cruise operation, a supersonic overspeed could result, leading to large wave-induced drag forces on the nacelle. The drag may be controlled by limiting the nacelle surface curvature, but this leads to a larger maximum diameter than would be optimum for cruise. Thus, it is the engine-out condition that limits the compactness of the nacelle, which has a direct bearing on cruise fuel economy. In addition, the windmilling drag has an impact on the size of the aircraft vertical stabilizer. Specifically, the moment on the aircraft caused by the loss of an engine at takeoff determines the vertical stabilizer size required to maintain yaw control [1].

Although the windmill condition is taken into account during the design the nacelle, it has received scant attention in designing the fan stage. Previous approaches to turbofan windmilling have employed either direct empirical scaling based on parameters such as the flight Mach number [2], or cycle matching based on component maps to predict performance [3,4]. However, since these methods provide no insight into the fan flow field at the windmill condition, we attempt, in the present study, to develop a better understanding of the fan stage flow by examining engine test data and through numerical simulation of a contemporary high bypass ratio turbofan.

We commence with an analysis of altitude test data acquired at various simulated flight Mach numbers, and show that the windmill rotational speed scales with the engine mass flow rate. By making use of the measured nozzle flow and thrust in conjunction with the known values of the nozzle coefficients, the stagnation pressure loss of the fan stage is determined and found to increase significantly as the flow increases.

In order to better understand the reasons for the observed behavior, numerical simulations of the fan stage are carried out, and the calculated overall stagnation pressure loss is found to be in good agreement with the test data. The simulations also enable the loss contributions of the various components to be determined. In addition, it is found that the normalized stagnation enthalpy change across the rotor is nearly zero, indicating that no work is done. This results in a nearly axial rotor exit absolute flow, which has major consequences. Specifically, since the vanes are designed to accept a rotor exit flow with the much greater swirl occurring at the cruise condition, a severe negative incidence results. This causes a massive separation to occur and large losses are generated.

Making use of the observation that the work done by the rotor is essentially zero, a simple model is developed to determine the fan rotational speed. Comparison of the model prediction with the test data shows good agreement. Moreover, the radial profiles of the flow quantities predicted by the model are found to agree well with the simulation results. This enables a procedure to be formulated for the determination of the internal drag of the propulsion system at windmill.

A meridional cross section of the flow configuration is illustrated in Fig. 1(*a*), in which the axial coordinate x and radial coordinate r are both normalized by the leading edge tip radius of

[1]This quantity is defined as the ratio of the capture streamtube area far upstream to the area at the nacelle highlight.

Contributed by the International Gas Turbine Institute of ASME for publication in the JOURNAL OF TURBOMACHINERY. Manuscript received August 26, 2008; final manuscript received September 3, 2008; published March 25, 2010. Review conducted by David Wisler. Paper presented at the ASME Turbo Expo 2008: Land, Sea and Air (GT2008), Berlin, Germany, June 9–13, 2008.

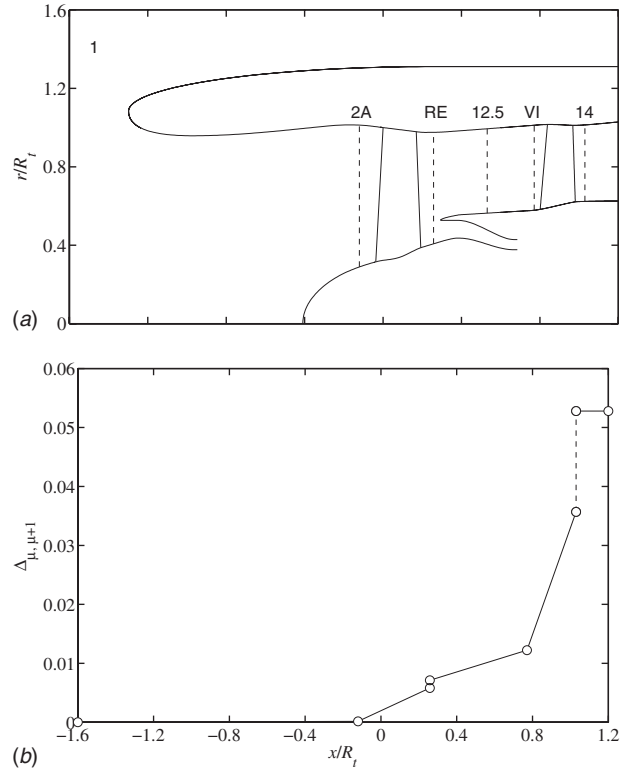

Fig. 1 (*a*) Notional meridional section of engine illustrating the stations used in the present study; (*b*) evolution of the normalized stagnation pressure loss through the fan stage for Φ =0.246

the fan R_t. The representation in Fig. 1(*a*) depicts notional rather than actual blade and vane geometries. Also shown in Fig. 1(*a*) are the locations of the engine stations that will be used in the subsequent analysis. The engine stations marked 1, 2A, 12.5, and 14 are the standard ones employed to indicate the free stream, rotor inlet, intrastage, and vane exit, respectively. In addition, we will find occasion to make use of the intermediate stations at the rotor exit (RE) and vane inlet (VI).

2 Engine Data Analysis

Windmill tests were carried out on the engine under condsideration in a simulated altitude facility. The inlet mass flow rate W_{2A}, fan rotational speed Ω, and gross fan nozzle thrust F were measured for values of the simulated flight Mach number M_1 between 0.4 and 0.8. By employing off-design component maps in system-level engine core simulations, the bypass ratios at these flight Mach numbers were estimated, enabling the flow split between the bypass and core streams to be determined. The bypass ratio over the entire range of M_1 was found to be an order of magnitude larger than it is at cruise. In the development that follows, ideal gas behavior with gas constant $\mathcal{R}$ and ratio of specific heats γ is assumed.

The fan tip speed $U_t=\Omega R_t$ is nondimensionalized by the free stream stagnation sonic speed $a_{T,1}=\sqrt{\gamma\mathcal{R}T_{T,1}}$, where T_T represents the stagnation temperature. Similarly, the windmilling mass flow rate is characterized by a dimensionless flow parameter Φ defined by

$$\Phi = \frac{W_{2A}(\mathcal{R}T_{T,1})^{1/2}}{p_{T,1}A_{2A}}$$

where p_T represents the stagnation pressure and A is the cross-sectional area. The nondimensional tip speed $U_t/a_{T,1}$ is shown in Fig. 2 as a function of the flight Mach number, as is the typical

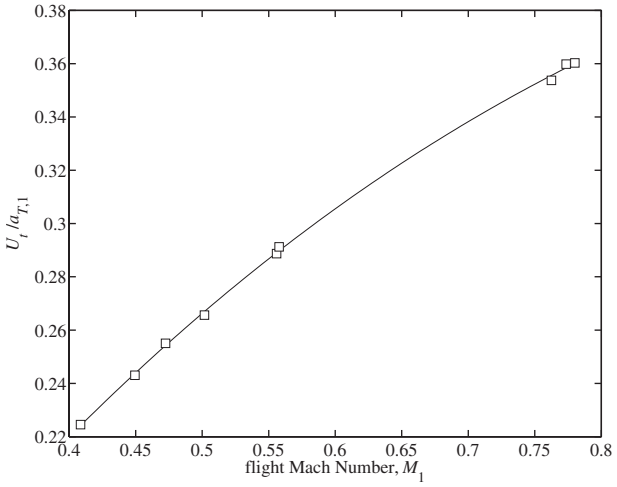

Fig. 2 Variation of dimensionless windmilling tip speed with flight Mach number

practice. We observe that the rotor speed grows with the flight Mach number, but appears to level off at larger values of M_1. On a physical basis, a direct connection between the windmilling speed and the flight Mach number is tenuous. Rather, one would expect the windmilling speed to depend on the mass flow rate through the engine. This hypothesis is examined in Fig. 3, in which the nondimensional tip speed is plotted as a function of the flow parameter Φ. It is observed that the correlation between the two quantities is essentially linear. This suggests that the fundamental parameter is not the flight Mach number, but rather the engine mass flow rate. The forward speed serves only to establish a ram pressure, which drives the flow through the engine. The magnitude of this flow depends on the losses in the fan stage, an aspect we turn to next.

The bypass duct of the engine studied here features a converging-diverging nozzle, the characteristics of which are known from scale-model tests. In particular, the coefficient of discharge C_D and that of gross thrust C_G referenced to Station 14 are known as functions of the fan nozzle stagnation-to-static pressure ratio $\xi=p_{T,14}/p_1$, enabling the internal stagnation pressure loss of the propulsion system to be estimated. The overall stagnation

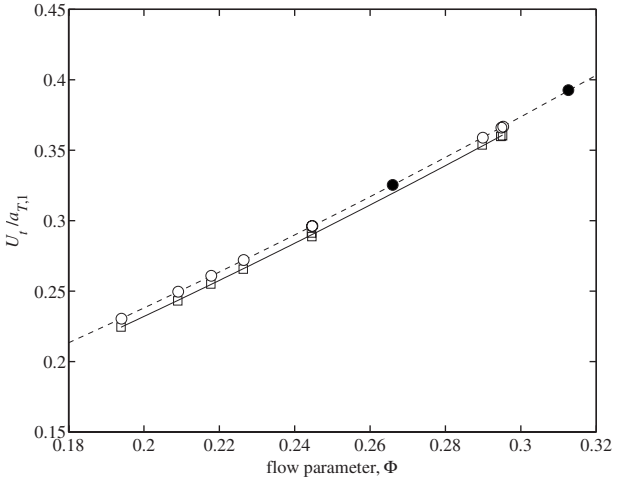

Fig. 3 Variation of dimensionless windmilling tip speed with flow parameter. Test data (□) and model predictions (○, ●) are shown, together with the corresponding lines of second-order best fit (——, – – –). The filled symbols indicate model predictions for points at which test data are not available.

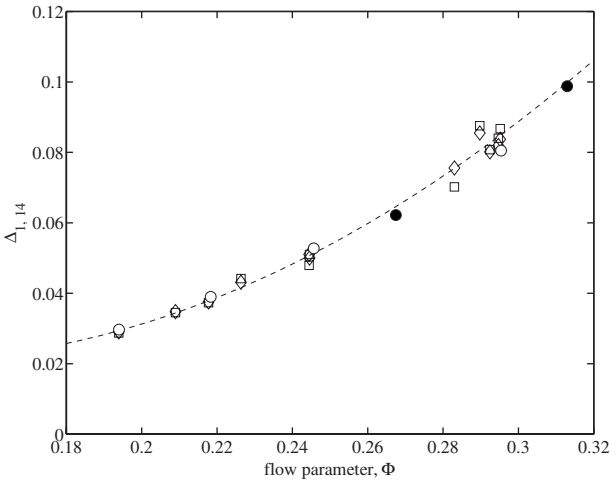

Fig. 4 Stagnation pressure loss as a function of flow parameter. Losses deduced from measurements of the mass flow rate (◇) and thrust (□) are shown. Simulation results for flow conditions based on the test data (○) and the present model (●) are also indicated. The line represents a second-order fit to the test data, and is extrapolated beyond the original range.

pressure loss of the internal flow can be represented as the sum of contributions from the inlet (1–2A), fan stage (2A–14), and aft duct/nozzle (14–nozzle exit). Anticipating that the inlet loss is negligible, $p_{T,14}$ can be determined from the known value of the bypass duct mass flow rate (W_{14}) using the following procedure.

The discharge coefficient is defined by $C_D = W_{14}/W_{\text{ideal}}$, where W_{ideal} is the ideal one-dimensional flow that would be obtained by isentropically expanding the flow through the nozzle at pressure ratio ξ. Making use of this definition, it follows that

$$C_D(\xi)[\xi^k(\xi^k - 1)]^{1/2} - \left[\frac{k\mathcal{R}T_{T,14}}{2}\right]^{1/2} \frac{W_{14}}{p_1 A_e} = 0 \tag{1}$$

where $k = (\gamma - 1)/\gamma$ and A_e is the nozzle exit area. Equation (1) can be solved by iteration to determine ξ and thus $p_{T,14}$, once $T_{T,14}$ is specified. In order to fix $T_{T,14}$, we note that, under steady windmilling conditions, the only work done by the fan is that required to overcome bearing friction and windage in the core. Since the losses associated with these mechanisms are small, it follows that, to first order, no work is done by the rotor. Further, there is no mechanism for energy addition or removal downstream of Station RE, so that we have $T_{T,14} = T_{T,\text{RE}} = T_{T,1}$ to a good approximation.

The stagnation pressure $p_{T,14}$ at the vane exit may also be determined by making use of the known values of the gross thrust coefficient $C_G = F/(W_{\text{ideal}} V_{\text{ideal}})$, where the denominator represents an ideal thrust, with V_{ideal} being the one-dimensional velocity that would be obtained by isentropically expanding the flow at Station 14 to the ambient pressure p_1. Neglecting the thrust due to the core stream, we obtain, analogous to Eq. (1)

$$C_G(\xi)[\xi^k - 1] - \frac{kF}{2p_1 A_e} = 0 \tag{2}$$

which can be solved to obtain a second estimate for $p_{T,14}$ independent of that obtained using Eq. (1).

Next, we define a normalized stagnation pressure loss between two stations μ and ν by

$$\Delta_{\mu,\nu} = \frac{p_{T,\mu} - p_{T,\nu}}{p_{T,1}}$$

and plot the overall loss $\Delta_{1,14}$ determined using both Eqs. (1) and (2) in Fig. 4 as a function of Φ. The agreement between the two sets of loss estimates is generally quite good, although the larger values of Φ exhibit greater differences. We also observe that at low values of Φ, the loss appears to scale almost linearly but grows rapidly as Φ increases. This is an interesting behavior that we explore next by numerical means.

3 Numerical Simulations

In the present study, the Reynolds-averaged Navier–Stokes equations for an ideal gas are solved numerically using the procedure developed by Davis et al. [5], based on the multiple grid scheme of Ni [6]. The algorithm employs centered second-order spatial differencing and second- and fourth-order smoothing. Turbulence closure is achieved using the k-ω model of Wilcox [7] and the quasi-two-dimensional nonreflecting conditions of Giles [8] are applied at the inflow and outflow boundaries. Domain decomposition and parallel capability permit large problems to be handled. The solver has been extensively validated for numerous turbomachinery applications, details of which may be found in the works of Ni and co-workers [9,10].

3.1 Numerical Model. The numerical model employed here is similar to that of Prasad and Feng [11], consisting of the fan, coupled to the bypass and core ducts downstream, and to an axisymmetric inlet upstream. However, unlike the configuration employed in Ref. [11], the fan exit guide vane is also included in the present simulations. The actual vane row is close-coupled with the pylon, necessitating the use of multiple vane classes with different degrees of camber so as to minimize back-pressure nonuniformities on the fan. An exact representation of this configuration would require a full wheel simulation, which would be prohibitively expensive. Instead, we choose to conduct the present simulations assuming axisymmetric vanes that provide the appropriate mean turning. This enables the use of single blade and vane passages, coupled via a mixing plane. A further complication arises due to the presence of large separated flow regions in the vane and over the splitter. It was found that this inhibits steady-state convergence, reflecting the physical tendency of the separated shear layers to become unstable. Since rotor-stator interaction is not the primary phenomenon of interest here, and since the unsteadiness occurs downstream of the rotor, transient simulations are carried out with the mixing plane inserted at Station RE, from which time-mean flow fields are determined. The simulations are run by setting the measured fan rotational speed and core and bypass duct flows to achieve an approximate solution, which is used to initialize the unsteady calculation. After the transient simulation has run sufficiently long that stationary conditions are achieved, an additional cycle is run in order to determine the average state.

3.2 Loss Predictions. We begin by examining the losses predicted by the simulations, and, to this end, it is necessary to first define an appropriate stagnation pressure to represent the flow at Station 14. The scale-model tests to determine the nozzle coefficients were carried out with a uniform stagnation pressure imposed at this station. In the present context, this is equivalent to presuming that any nonuniformities in the flow field at the vane exit are completely mixed out at Station 14. In reality, the mixing takes place continuously between the trailing edge of the fan exit guide vane and the nozzle exit, so that this way of accounting for the losses, while convenient, must be regarded as an approximation. For the present discussion, we take $p_{T,14}$ to be the fully mixed-out state defined by Pianko and Wazelt [12] and Prasad [13], which, by considering both radial and circumferential mixing, maintains consistency with the measurement procedure for C_D and C_G.

The normalized overall stagnation pressure loss $\Delta_{1,14}$ determined from the time-averaged simulations is shown in Fig. 4 as a function of the flow parameter Φ for conditions corresponding to four test points. The numerical results agree quite well with the data, particularly in view of the assumptions that have been made in reducing the test data and the approximations made in con-

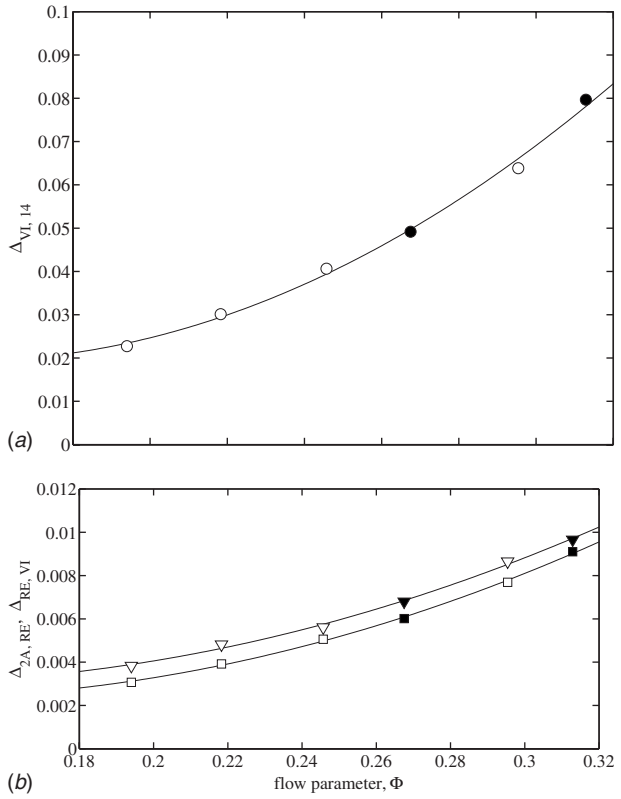

Fig. 5 Stagnation pressure losses across (*a*) the vane, and (*b*) the rotor (▽) and splitter (□) as a function of the flow parameter Φ. The lines represent second-order best fits, while the filled symbols indicate model predictions for points without corresponding test data.

structing the numerical model. Furthermore, intrastage instrumentation that was present during the tests would be expected to have led to an overestimate of the losses.

Next, we examine the evolution of the loss through the fan stage. For this purpose, we employ the entropy-averaged stagnation pressure, which, under steady flow conditions, preserves the entropy-flux of the nonuniform state [14]. We note, parenthetically, that when the entropy-averaged values were replaced with the more conventional mass-averaged ones, the results did not differ to any significant extent.

The development of the computed incremental losses between consecutive stations is traced in Fig. 1(*b*) for the operating condition with $\Phi=0.246$. As anticipated, the inlet loss ($\Delta_{1,2A}$) is insignificant. The loss across the rotor ($\Delta_{2A,RE}$), including the mixing loss of the rotor wakes, is about 0.6%, while that across the splitter ($\Delta_{RE,VI}$) is about 0.5%. The bulk of the loss occurs across the stator ($\Delta_{VI,14}$), accounting for about 4.1% in total. Of this, the vane passage contributes to 2.4%, while the wake mixing that occurs behind the stator accounts for the remaining 1.7%.

The behavior of the primary loss components is shown in Fig. 5 as a function of Φ. The general trends are very similar to those observed in Fig. 1(*b*); the dominant loss occurs in the stator, while the rotor and splitter contribute equally to the loss, albeit to a much lesser extent.

3.3 Rotor Flow Field. The generally good agreement between the test data and the numerical results suggests that the present simulation method captures the essential physics of the fan system flow. We therefore turn the attention to the features of this flow, and begin by examining the work done across the rotor, which is quantified by means of a nondimensional work coefficient, defined according to

Table 1 Numerically determined rotor work coefficient at windmill and ground idle conditions

M_1	Φ	Ψ
0.780	0.295	-2.83×10^{-5}
0.556	0.246	-2.67×10^{-4}
0.472	0.218	-1.38×10^{-4}
0.409	0.194	-1.58×10^{-4}
Idle	0.123	8.97×10^{-3}

$$\Psi = \frac{C_p(T_{T,\mathrm{RE}} - T_{T,2\mathrm{A}})}{U_t^2}$$

where C_p is the specific heat at constant pressure. The values of Ψ for the four test conditions are shown in Table 1, and are observed to be quite small. As a means of placing these these values in perspective, the work coefficient at the ground idle condition is also displayed in Table 1, and is found to be nearly two orders of magnitude larger than at the windmill conditions. We therefore conclude that, to a good approximation, no work is done by the rotor.

Next, in preparation for studying the rotor flow, a typical velocity triangle is illustrated in Fig. 6. The axial and tangential directions are indicated by x and θ, respectively, and the relative and absolute swirl angles β and α are measured in the counterclockwise direction relative to the x-axis. Radial profiles of the circumferentially-averaged relative flow angle β at Station RE are shown in Fig. 7(*a*) for the four flow conditions studied. The β profiles are observed to be essentially independent of the specific windmill operating condition, particularly in the outer span, away from the splitter, the leading edge of which lies at $r/R_t=0.53$. Also shown in Fig. 7(*a*) is the nominal blade exit metal angle β^*. The numerical profiles of β appear to follow the values of β^* in the outer span, although some differences are apparent. If the flow deviation, δ is accounted for using Carter's Rule [15], the resulting flow angle $\beta^*+\delta$ is observed to be in better agreement with the numerical profiles. In view of the fact that Φ varies significantly over the four flow conditions, it would appear that the relative flow angle is set only by the blade geometry, independent of the specific windmill condition.

Turning now to the absolute flow angle, we examine in Fig. 7(*b*) the radial profiles of α at Station RE. Again, it is observed that the profiles are nearly identical for the four cases. The region corresponding to the bypass duct is one of relatively small abso-

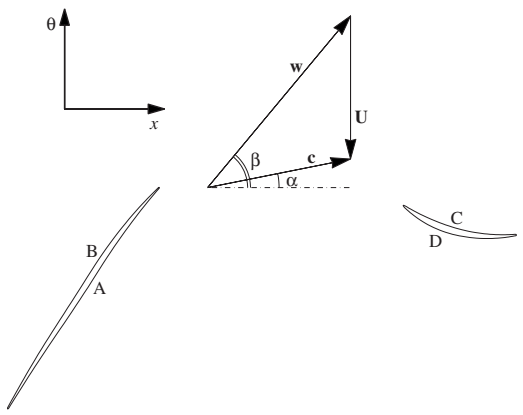

Fig. 6 Velocity triangle and angle convention used in the present analysis. The relative and absolute velocities are denoted by *w* and *c*, respectively, and the wheel velocity by *U*. Flow angles are measured counterclockwise from the positive *x*-axis.

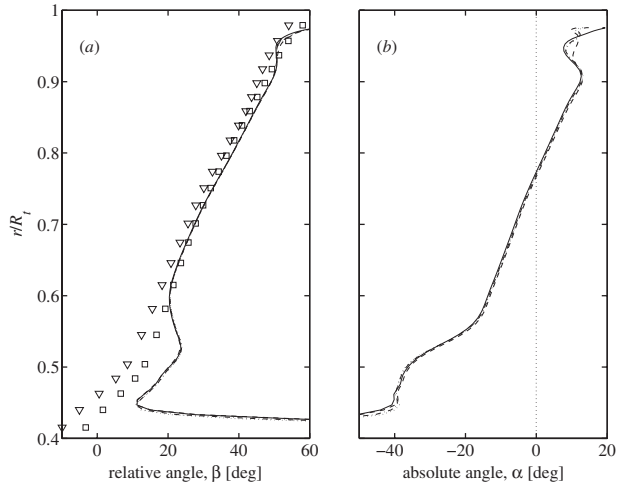

Fig. 7 Circumferentially-averaged rotor exit radial profiles of (*a*) relative swirl angle β, and (*b*) absolute swirl angle α with $\Phi=0.295$ (——), $\Phi=0.246$ (– – –), $\Phi=0.218$ (–·–·–), and $\Phi=0.194$ (·····). Also shown in (*a*) are the nominal blade exit metal angle β^* (▽) and the relative flow angle estimated by applying Carter's rule (□).

lute swirl, with $|\alpha|<10$ deg over most of the outer span. Furthermore, its value changes sign at $r/R_t=0.77$. Since the flow entering the blade has zero absolute swirl, it follows that the blade sections outboard of the section at $r/R_t=0.77$ operate in a turbine mode by extracting work from the flow, while those inboard of this section operate in a compressor mode by doing work on the flow. In view of the previous results concerning the rotor work coefficient, it is evident that the two types of work essentially cancel each other.

Next, we turn the attention to circumferentially-averaged profiles of the stagnation temperature at Station RE, which are plotted, normalized by $T_{T,1}$ in Fig. 8 for the conditions listed in Table 1. The profile shapes are similar for all four cases, exhibiting a stagnation temperature deficit in the outer part of the annulus and a surplus in the inner part. This is in accord with the previous observation that the outer sections of the blade operate in a turbine mode, while the inner ones perform compression work. More quantitatively, we note that the profiles cross unity at $r\approx0.77$, which corresponds to the location at which the absolute flow is swirl-free. Finally, we note that, although the profiles in Figs. 7

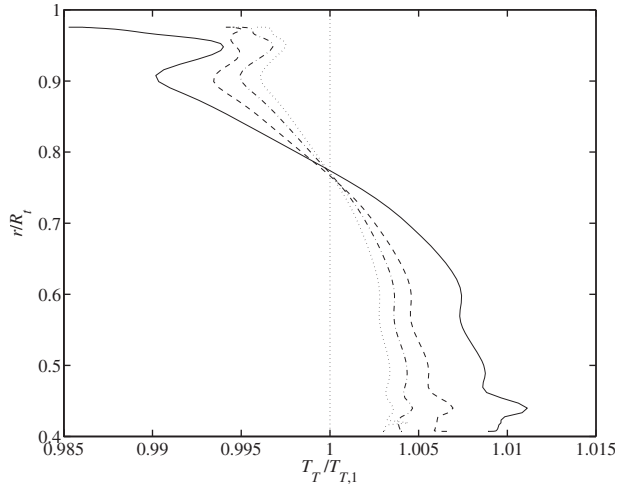

Fig. 8 Circumferentially-averaged radial profiles of the normalized stagnation temperature at the rotor exit with $\Phi=0.295$ (——), $\Phi=0.246$ (– – –), $\Phi=0.218$ (–·–·–), and $\Phi=0.194$ (·····)

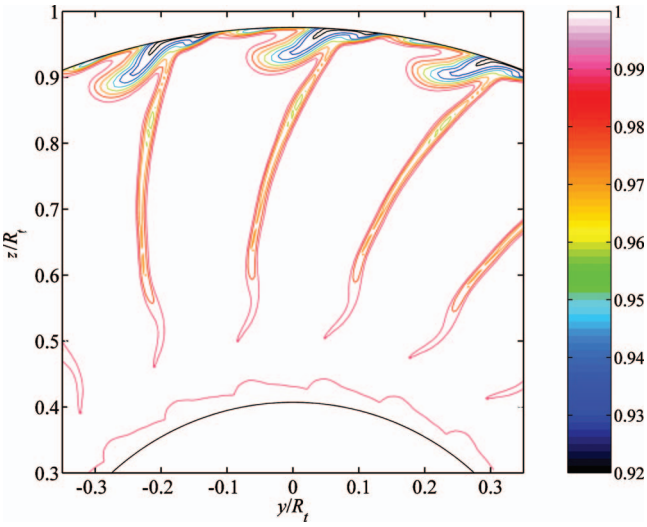

Fig. 9 Rotary stagnation pressure at Station RE for $\Phi=0.246$

and 8 are generally smooth, a nonuniformity occurs near $r/R_t=0.9$. In order to better understand this behavior, it is necessary to examine the flow field in more detail.

This is done in Fig. 9, which depicts the rotary stagnation pressure [14] field at Station RE, normalized by $p_{T,1}$ for the case $\Phi=0.246$. For isentropic steady flow through the rotor, this quantity should be unity, and values less than 1 indicate the presence of losses. We observe that some losses are generated on the endwalls and in the wakes, as expected. The wakes themselves are relatively thin over most of the span. However, there is evidently a region of significant loss that occurs in the vicinity of $r/R_t=0.9$, corresponding to the location of the anomalous behavior in the radial profiles of the flow angles and stagnation temperature.

An examination of Fig. 10 serves to clarify the reason for the increase in loss near $r/R_t=0.9$. Here, we illustrate the relative Mach number field on blade-to-blade computational planes at 85% and 40% span, which correspond to blade trailing edge values of r/R_t of 0.9 and 0.63, respectively. On the latter plane, we observe that the flow enters the blade with a mild negative incidence, stagnating on the surface marked B in Fig. 6. Under powered operation, this would be the suction surface of the blade. Despite the negative incidence, the blade flow field at 40% span is well behaved. However, at 85% span, the incidence is severely negative, causing separation off the surface, indicated as A in Fig. 6. It is this separation that generates the large loss and causes the nonuniformities in the flow angle and stagnation temperature profiles.

We have thus far alluded only briefly to the splitter and its effect on the rotor flow. In view of the large bypass ratios at the windmill condition, it is expected that the flow will enter the splitter at a large angle of attack, leading to separation. This is confirmed by the simulations, as seen in Fig. 11(*a*), in which the circumferentially-averaged normalized stagnation pressure profile at Station 12.5 is shown for the $\Phi=0.246$ case. In the region $r/R_t>0.65$, the shape of the profile is similar to that in Fig. 8. However, for $r/R_t<0.65$, a significant deficit is observed, indicating the presence of a large separation. Also shown in Fig. 11(*a*) are test data acquired at this engine station. We note that although the two profiles are qualitatively similar, there are also major differences. These differences may be understood by examining Fig. 11(*b*), in which the circumferentially-averaged absolute flow angle is plotted together with the angle setting of the stagnation pressure probes. It is observed that the probes, which were positioned to measure the flow properties at the aerodynamic design point, operate at a large incidence to the flow over most of the annulus. For $0.65<r/R_t<0.75$, where the flow incidence on the probe is rela-

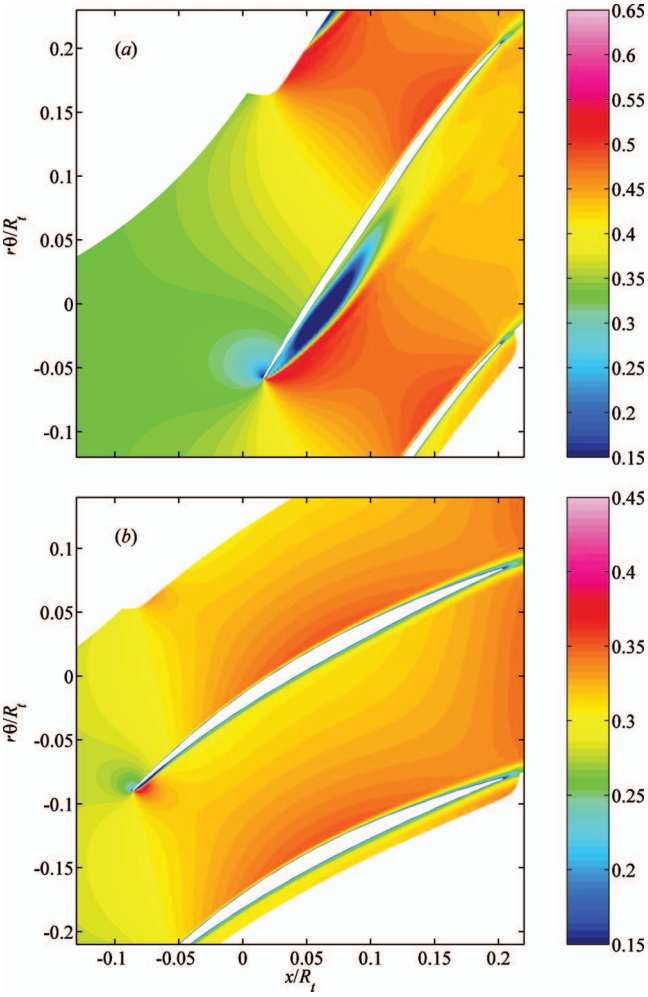

Fig. 10 Computed blade relative Mach number field at (*a*) 85% span and (*b*) 40% span for Φ=0.246

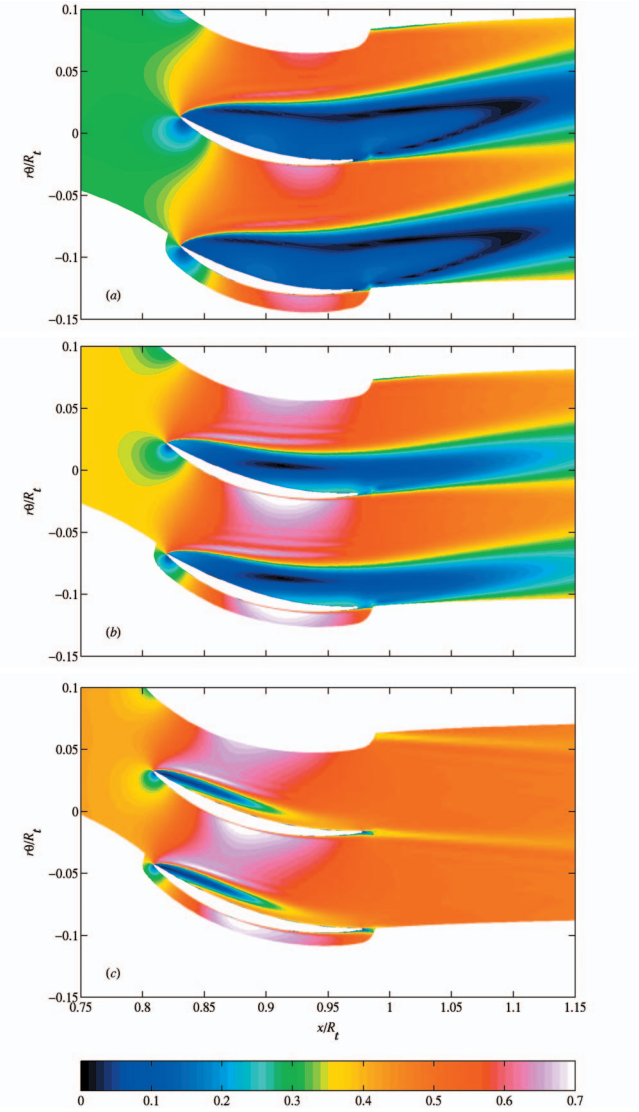

Fig. 12 Computed vane Mach number field at (*a*) 80% span, (*b*) 50% span, and (*c*) 20% span for Φ=0.246

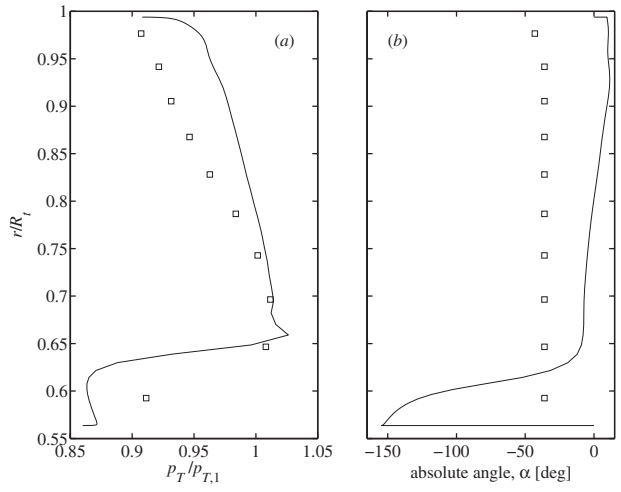

Fig. 11 (*a*) Numerical (——) and measured (□) stagnation pressure radial profiles at Station 12.5 for Φ=0.246; (*b*) numerically determined (——) absolute flow angle and probe angle (□) as functions of radius

tively small, the simulation results agree quite well with the data. In other parts of the flow, where the incidence is higher, one would expect the recovery of the probe to be poor, leading to a lower measured value of the stagnation pressure.

3.4 Vane Flow Field. We now direct attention to the vane flow, where, according to the results presented in Figs. 1 and 5, the bulk of the loss is generated. Since the efficiency of the fan stage at the cruise condition is paramount, the vane is designed to minimize the flow incidence at this condition. The nominal metal angle at the leading edge is therefore about −40 deg over most of the span. On the other hand, as was observed previously, the absolute flow leaves the rotor with a small degree of swirl, leading to a strong negative incidence on the vane. This feature is apparent in Fig. 12, which depicts the vane-to-vane Mach number field on radial computational planes located at span fractions of 0.8, 0.5, and 0.2 for Φ=0.256. At all three spans, we observe that the flow stagnates on the surface indicated as D in Fig. 6, which would be the suction surface under powered operation. The effect of this large negative incidence is to cause the flow at the 80% span location to separate at the leading edge and to remain separated over the surface referred to as C in Fig. 6 (normally the pressure surface of the vane). The flow separation is so large that

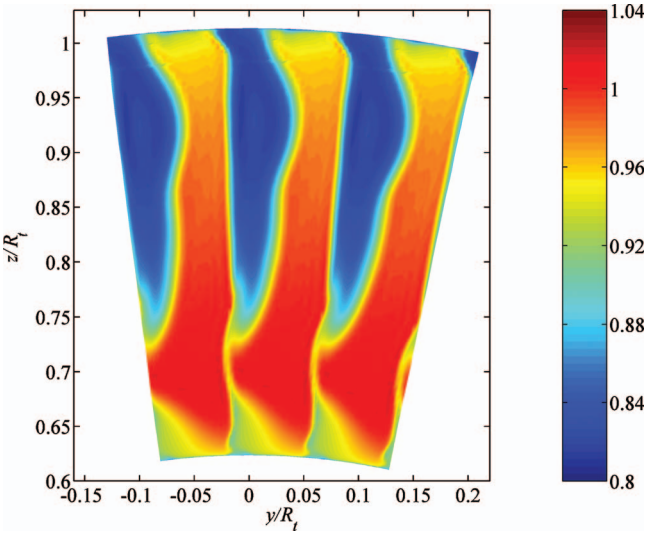

Fig. 13 Normalized stagnation pressure at Station 14 for Φ =0.246. The large blockage caused by the flow separation is evident.

an alternating wake jet structure is formed downstream of the vane. The incidence decreases in severity at lower spans, consistent with the flow angle behavior shown in Fig. 7. At 20% span, we observe that the separated flow reattaches roughly at midchord, resulting in a significantly smaller wake.

The overall behavior of the wake at Station 14 is presented in Fig. 13 in terms of the stagnation pressure normalized by $p_{T,1}$. The blockage caused by the flow separation is observed to be very large, and occupies nearly half the passage width in the outer span of the vane. Near the hub, a small stagnation pressure deficit due to secondary flow is observed. The presence of large regions of separated flow explains the high losses in the vane. Moreover, the mixing out of the alternating wake jet structure downstream of the vane leads to additional losses. Returning to Fig. 12, we observe that although the flow separation increases with span, the local flow speeds are greatest at the lower spans. This is because the vane spacing is smallest at the lower span so that even a relatively small blockage of the flow passage there leads to elevated Mach numbers.

This effect is quantified in Fig. 14, which depicts the surface isentropic Mach number M_{is} at the three spanwise locations of Fig. 12. At 20% span, the highest value of M_{is} is 0.74, while at 80% span, it does not exceed 0.65. These values of M_{is} are surprisingly large, and it is worthwhile to examine the behavior of this quantity as Φ is increased. The results obtained from simulations carried out with $\Phi=0.295$ are illustrated in Fig. 14, where we observe that although M_{is} increases at 80% span, it remains subsonic. At 50% and 20% span, the flow accelerates to locally supersonic values of M_{is} before returning to a subsonic state. In the former case, the subsonic transition is shockless, whereas in the latter case, the flow returns to a subsonic state across what appears to be a weak shock. In order to ascertain this behavior, it is of interest to inquire into the nature of the flow field at still higher values of Φ. However, since no test data are available for $\Phi>0.295$, the windmilling speed to be specified in the simulation must be determined by other means. A model to accomplish this is described in the Sec. 4, and the results of a calculation carried out with $\Phi=0.313$ are shown in Fig. 14. It is evident that the vane flow field now features a shock across most of its span. Normally, the presence of shocks in turbomachine blade passages is associated with choking, where reductions in the back pressure are accompanied by a rapid increase in the loss owing to an increase in the shock strength. However, this behavior cannot be expected to be true in the present situation, where the flow restriction is

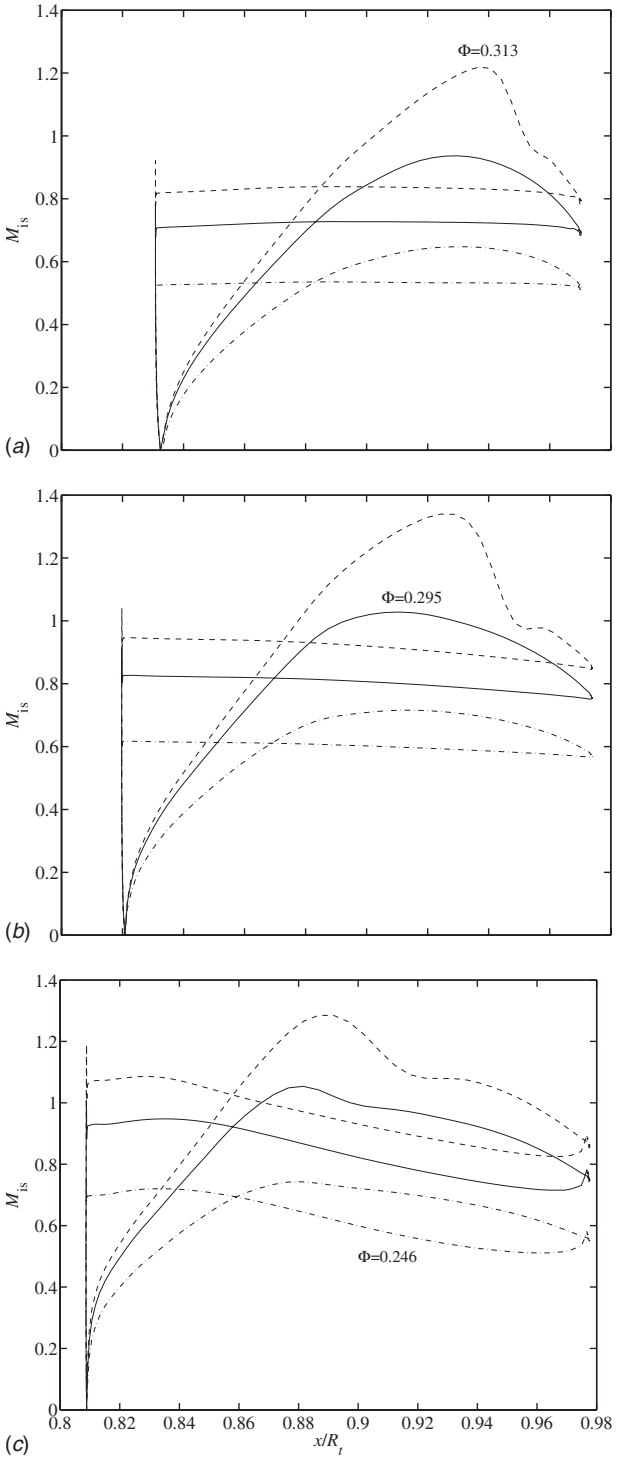

Fig. 14 Vane isentropic Mach number at (*a*) 80% span, (*b*) 50% span, and (*c*) 20% span for Φ=0.246 (–·–·–), Φ=0.295 (——), and Φ=0.313 (– – –)

caused, not by the geometrical characteristics of the vane but rather by the occurrence of the flow separation, which is itself altered by changes in the back pressure.

4 Windmill Rotational Speed Model

The development thus far has focused on the nature of the flow field and associated losses in the fan stage. The simulations were carried out with the windmill rotational speed Ω being prescribed from test data. However, this quantity is not known during the

design phase of a new engine, and the method of scaling alluded to previously may prove to be unreliable, especially when the new engine employs a different design philosophy. On the other hand, optimization of the propulsion system requires simulations of the type described in the present study, making it necessary to deduce the windmill speed using only parameters that are available early in the design cycle. This issue is addressed here by formulating a simple physical model to determine the fan's rotational speed at any given windmilling mass flow rate.

As we have noted previously, the flow leaves the blade at an angle that is well approximated over the outer span of the blade by $\beta=\beta^*+\delta$, which is determined solely by the blade geometry. We now assume that the absolute flow behind the rotor is steady, that it is a function only of r, and that the radial component of the velocity is negligible compared to its axial and tangential counterparts, which results in mass conservation being satisifed automatically. Since the absolute flow enters the blade without swirl, application of the Euler turbine equation across the rotor yields

$$C_p(T_T - T_{T,2A}) = -r\Omega c_\theta \tag{3}$$

Further, denoting the absolute velocity vector by c and assuming isentropic flow in the rotor, it follows from Crocco's theorem [14] that

$$c \times (\nabla \times c) = C_p \nabla T_T$$

which, when applied to the present situation, yields

$$c_x \frac{dc_x}{dr} + \frac{c_\theta}{r}\frac{d}{dr}(rc_\theta) = C_p \frac{dT_T}{dr} \tag{4}$$

Eliminating T_T from Eqs. (3) and (4), we obtain

$$\frac{1}{r}(c_\theta + r\Omega)\frac{d}{dr}(rc_\theta) = -c_x \frac{dc_x}{dr} \tag{5}$$

From the velocity triangle in Fig. 6, it is evident that

$$c_\theta = c_x \tan\beta - r\Omega$$

Making use of this relationship between the axial and tangential components of velocity in Eq. (5), we obtain, after some simplification,

$$\frac{dc_x}{dr} + \left[\frac{\sin 2\beta}{2r}\frac{d}{dr}(r\tan\beta)\right]c_x = \Omega \sin 2\beta \tag{6}$$

Assuming that $c_x=c_{x,s}$ and $\beta=\beta_s$ at the splitter radius R_s, Eq. (6) can then be integrated to yield

$$c_x = \mathcal{F}^{-1}\cos\beta\left[c_{x,s}\sec\beta_s + 2\Omega\int_{R_s}^{r}\mathcal{F}\sin\beta dr\right] \tag{7}$$

where

$$\mathcal{F} = \exp\left(\int_{R_s}^{r}\frac{\sin^2\beta}{r}dr\right)$$

It is evident that the quantities $c_{x,s}$ and Ω in Eq. (7) must be specified in order to determine the axial velocity profile $c_x(r)$. The presence of two unkown quantities requires two equations, which we now derive from the prescription of the bypass duct mass flow rate and the constraint of zero work across the rotor. We note first that Eq. (3) can be cast in the form

$$\frac{T}{T_{T,2A}} = 1 - \left(\frac{\gamma-1}{2a_{T,2A}^2}\right)(c_x^2 + c_\theta^2 + 2r\Omega c_\theta) \tag{8}$$

thus, determining the static temperature. Upon invoking the assumption of isentropic flow, the density downstream of the rotor is given by

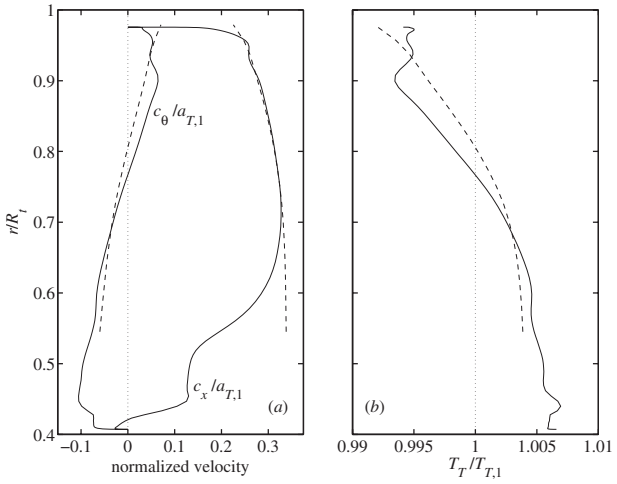

Fig. 15 Comparison of rotor exit (*a*) velocity and (*b*) stagnation temperature profiles obtained using the present model (– – –) with those obtained from the simulations (——) at $\Phi=0.246$

$$\rho = \rho_{T,2A}\left(\frac{T}{T_{T,2A}}\right)^{1/(\gamma-1)}$$

Taking the bypass duct mass flow rate to be $\dot{m}_b$, we require that

$$2\pi\int_{R_s}^{R_b}\rho c_x r dr = \dot{m}_b \tag{9a}$$

where R_b is the outer radius of the fan at the trailing edge. Similarly, making use of Eq. (3), the requirement of zero net work across the rotor yields

$$\int_{R_s}^{R_b}\rho c_x(r\Omega - c_x\cot\beta)r^2 dr = 0 \tag{9b}$$

Since no work is done on the fluid upstream of the rotor, we have $T_{T,2A}=T_{T,1}$. In addition, the numerical results have shown that the inlet losses are negligible, so that $\rho_{T,2A}=\rho_{T,1}$. Hence, Eqs. (9*a*) and (9*b*) can be solved by Newton iteration to determine the two unknowns $c_{x,s}$ and Ω. The values of $U_t/a_{T,1}$ thus determined are plotted in Fig. 3 for the points corresponding to the conditions at which the test data were acquired. Despite a small overprediction of the windmill speed, good agreement with the measured data is observed, which suggests that the model captures the basic phenomena correctly. In order to assess the veracity of the model in more detail, we compare the radial profiles of the normalized velocity components $c_x/a_{T,1}, c_\theta/a_{T,1}$ and that of the normalized stagnation temperature $T_T/T_{T,1}$ at the rotor exit in Fig. 15. The agreement is still remarkably good, with the greatest deviation being observed to occur in the axial velocity profile near the splitter, where the radial velocity is largest. The zero-swirl station predicted by the model occurs slightly more outboard than in the simulation results, and this is also reflected in the behavior of the stagnation temperature.

These results enable a sufficient degree of confidence in the present model to employ the predicted value of Ω in simulations of flow conditions for which no test data are available. To begin with, we consider the case $\Phi=0.266$, which lies within the range of the test data. The numerically predicted loss at this condition, shown in Fig. 4, follows the trend of both the test data and the previous simulations. Considering next a much higher flow case with $\Phi=0.313$, we find that the loss is quite high, with a value of nearly 10%, but consistent with the general trend. In both cases,

the values of Ψ were found to be small, indicating that the zero-work approximation assumed in deriving the windmill speed model holds for the simulations as well.

A further approximation that sheds more light on the quantities determining Ω can be developed. Observing from Fig. 15(*a*) that the axial velocity variation in the bypass duct is relatively weak, we may approximate c_x by a constant value, say $\bar{c}_x$. Moreover, in view of the fact that $c_\theta \ll c_x$, the terms on the right hand side of Eq. (8) involving c_θ may be dropped, so that $\bar{c}_x$ is determined by solving the analog of Eq. (9*a*)

$$\frac{\bar{c}_x}{a_{T,1}}\left[1-\frac{\gamma-1}{2}\left(\frac{\bar{c}_x}{a_{T,1}}\right)^2\right]^{1/(\gamma-1)}=\frac{\dot{m}_b}{\rho_{T,1}a_{T,1}\pi(R_b^2-R_s^2)}$$

Applying the same approximations to Eq. (9*b*), we then find that

$$\Omega=\frac{4\bar{c}_x}{R_b^4-R_s^4}\int_{R_s}^{R_b} r^2\cot\beta dr$$

showing the direct relationship between the mean duct velocity and the windmill rotational speed. Furthermore, it is evident that the blade exit flow angle distribution plays a signficant role in determining Ω.

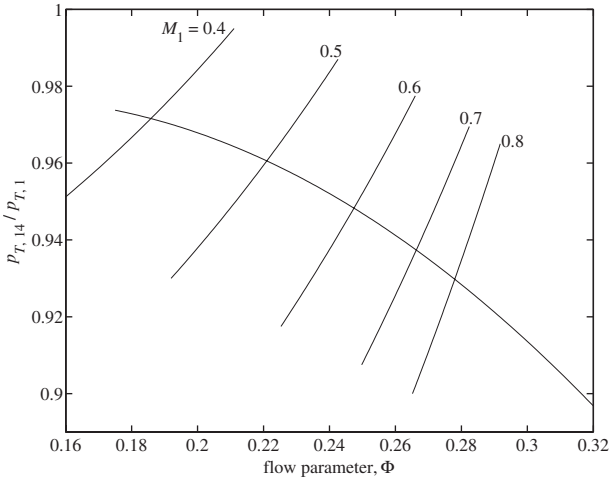

Fig. 16 Illustration of fan stage stagnation pressure loss and nozzle characteristics. The fan operating condition at any given flight Mach number occurs at the intersection of the corresponding nozzle characteristic and the fan loss characteristic.

5 Discussion

In the present study, we have undertaken an investigation of a high-bypass ratio turbofan stage at the engine-out windmill condition through the examination of test data and through numerical simulations. It was shown from the data that the windmill rotational speed scales with a corrected mass flow rate parameter, and that the stagnation pressure loss across the fan stage rises significantly with this corrected flow parameter. Numerical simulations of the fan stage were shown to provide a good estimate of the loss, and revealed that a substantial portion of it was incurred across the vane. Furthermore, the relative flow was shown to leave the rotor at very nearly the blade metal angle, independent of the corrected flow parameter. The absolute flow was found to possess only a weak swirl, with the outer sections of the blade operating in a turbine mode, and the inner sections as a compressor, so that the overall work is essentially zero. The low-swirl flow enters the stator at a severely negative incidence over most of its span, leading to a massive separation, thereby inducing large losses.

A simple model for the windmill rotational speed, developed on the basis of the flow features observed in the simulations, was found to match the test data well. In this model, the rotational speed is governed by the mass flow rate and by the blade relative flow exit angle. The intent of the model is to predict the windmill rotational speed to be employed in numerical simulations of the fan stage, without the need for carrying out tests. In particular, a fan stage loss characteristic may be generated as shown in Fig. 16, which depicts the fan stage stagnation pressure ratio $p_{T,14}/p_{T,1}$ as a function of the corrected flow parameter Φ. This characteristic bears a superficial resemblance to a constant speed line for a powered fan, but it should be emphasized that it is a line of constant (zero) work. Also shown in Fig. 16 are the nozzle characteristics for different flight Mach numbers, which can be determined once the discharge coefficient has been specified. The fan stage operating condition at any given flight Mach number is then determined by the intersection of the nozzle characteristic at that Mach number with the fan stage loss characteristic. This intersection point provides both the windmill rotational speed and the fan stage stagnation pressure ratio, which enables the internal drag of the propulsion system to be determined.

Finally, we turn to the issue of flow spillage over the nacelle that was alluded to in Sec. 1. The isentropic Mach number distributions over the inlet portion of the nacelle surface are illustrated in Fig. 17 for the four simulated windmill conditions in Table 1. The flow stagnates on the inner surface at $x/R_t \approx -1.25$, and the large curvature near the nacelle leading edge results in high local flow acceleration. Thus, we observe that for the $M_1 = 0.409$ case, a peak isentropic Mach number of nearly 0.8 is achieved on the outer surface. This value rises to 0.93 for $M_1 = 0.472$, and, as the flight Mach number is increased to 0.556, the flow becomes locally supersonic, transitioning to the subsonic state across a weak shock that is formed at $x = -1.27$. At the highest flight Mach number of 0.78, the flow accelerates to an even greater extent and forms an even stronger shock that occurs further aft on the nacelle. The drag associated with a shock of this type can be expected to be considerable.

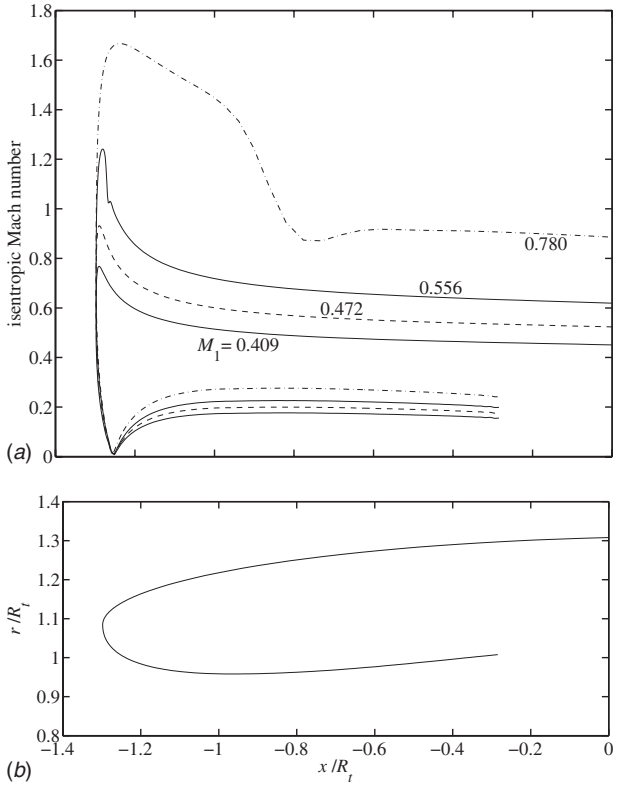

Fig. 17 Isentropic Mach number distribution (top) over the nacelle surface (bottom) at the windmill conditions listed in Table 1

Acknowledgment

The authors are grateful to Pratt and Whitney for granting permission to publish the present work. They are also indebted to S. Morford for suggesting the present study and for several fruitful discussions on this subject.

Nomenclature

A = duct cross-sectional area
a_T = stagnation sonic speed
α = absolute flow angle
$\mathbf{c}$ = absolute velocity
β = relative flow angle
C_D = nozzle discharge coefficient
C_G = nozzle gross thrust coefficient
C_p = specific heat at constant pressure
Δ = normalized stagnation pressure loss
F = nozzle thrust
γ = specific heat ratio
M = Mach number
p = static pressure
p_T = stagnation pressure
Φ = flow parameter
r = radial coordinate
ρ = density
T_T = stagnation temperature
θ = circumferential coordinate
Ω = fan rotational speed
R_b = fan trailing edge outer radius
R_s = splitter radius
R_t = fan leading edge tip radius
$\mathcal{R}$ = gas constant
U_t = fan tip speed
W = mass flow rate
x = axial coordinate
ξ = fan nozzle stagnation-to-static pressure ratio

References

[1] Daggett, D.L., Brown, S.T., and Kawai, R.T., 2003, "Ultra-Efficient Engine Diameter Study," NASA Report No. CR 2003-212309.
[2] Walsh, P. P., and Fletecher, P., 2004, *Gas Turbine Performance*, Blackwell Science, Oxford, UK.
[3] Anderson, B. A., Messih, D., and Plybon, R. C., 1997, "Engine-Out Performance Characteristics," ISABE Paper No. 97–7216.
[4] Braig, W., Schulte, H., and Riegler, C., 1999, "Comparative Analysis of the Windmilling Performance of Turbojet and Turbofan Engines," J. Propul. Pow., **15**, pp. 326–333.
[5] Davis, R.L., Ni, R.-H., and Carter, J.E., 1986, "Cascade Viscous Flow Analysis Using the Navier–Stokes Equations," AIAA Paper No. 86–0033.
[6] Ni, R.-H., 1982, "A Multiple-Grid Scheme for Solving the Euler Equations," AIAA J., **20**, pp. 1565–1571.
[7] Wilcox, D. C., 1998, *Turbulence Modeling for CFD*, DCW Industries, Inc., La Canada, CA.
[8] Giles, M. B., 1990, "Non-Reflecting Boundary Conditions for Euler Equation Calculations," AIAA J., **28**, pp. 2050–2058.
[9] Ni, R.-H. and Bogoian, H., 1989, "Predictions of 3-D Multi-Stage Turbine Flow Fields Using a Multiple-Grid Euler Solver," AIAA Paper No. 89-0233.
[10] Ni, R.-H. and Sharma, O.P., 1990, "Using a 3-D Euler Flow Simulation to Assess Effects of Periodic Unsteady Flow Through Turbines," AIAA Paper No. 90-2357.
[11] Prasad, D., and Feng, J., 2005, "Propagation and Decay of Shock Waves in Turbofan Engine Inlets," ASME J. Turbomach., **127**, pp. 118–127.
[12] Pianko, M. and Wazelt, F., 1983, "Suitable Averaging Techniues in Non-Uniform Internal Flows," Propulsion and Energetics Panel Working Group 14, Paper No. AGARD AR 182.
[13] Prasad, A., 2005, "Calculation of the Mixed-Out State in Turbomachine Flows," ASME J. Turbomach., **127**, pp. 564–572.
[14] Greitzer, E. M., Tan, C. S., and Graf, M. B., 2004, *Internal Flow: Concepts and Applications*, Cambridge University Press, Cambridge, UK.
[15] Cumpsty, N. A., 1989, *Compressor Aerodynamics*, Longman, Harlow, UK.